Journal of Food Engineering 403 (2026) 112725

Contents lists available at ScienceDirect

Journal of Food Engineering

journal homepage: www.elsevier.com/locate/jfoodeng

A novel quantitative analysis method for printability in 3D food printing for surimi

Sol Kim [a], Jaehwi Seol [b,c], Eunji Ju [b,c], Jeonghyeon Pak [b,c], Hyoung Il Son [b,c,d,*], Soo-Jung Kim [a,d,**]

[a] Department of Integrative Food, Bioscience and Biotechnology, Chonnam National University, Gwangju, 61186, Republic of Korea
[b] Department of Convergence Biosystems Engineering, Chonnam National University, 77 Yongbong-ro, Buk-gu, Gwangju, 61186, Republic of Korea
[c] Interdisciplinary Program in IT-Bio Convergence System, Chonnam National University, 77 Yongbong-ro, Buk-gu, Gwangju, 61186, Republic of Korea
[d] Research Center for Biological Cybernetics, Chonnam National University, 77 Yongbong-ro, Buk-gu, Gwangju, 61186, Republic of Korea

ARTICLE INFO

Keywords:
Three-dimensional food printing
Water holding capacity
Gel strength
Image processing
Gray-level Co-Occurrence matrix
Machine learning

ABSTRACT

The success of 3D food printing (3DFP) relies heavily on material printability, defined by smooth extrusion and structural stability. However, many food materials struggle to meet these criteria, leading to challenges in shaping and printing precision. Conventional evaluation methods for evaluating key printability indicators like water holding capacity (WHC) and gel strength are often costly, require specialized equipment, and are destructive. To overcome these limitations, this study proposes a non-destructive, computer vision-based approach for printability evaluation using digital images. Grayscale images were analyzed to extract texture features based on the gray-level co-occurrence matrix (GLCM). These texture features, along with additive concentration data, then served as input for a Random Forest model. Three distinct models were developed: top view (TOP), side view (SIDE), and combined view (TS). The TOP model demonstrated the highest predictive performance for WHC (MAE = 0.674, R^2 = 0.875, RMSE = 0.831), while the TS model showed superior accuracy for gel strength (MAE = 0.391, R^2 = 0.691, RMSE = 0.556). This novel approach enables rapid, automated, and cost-effective assessments, thereby significantly aiding in 3DFP optimization and the development of customized food products.

1. Introduction

Three-dimensional (3D) printing is a technology that constructs complex solid models by incrementally layering materials from the bottom upward, following predefined digital designs under precise computer control. This technology has been widely employed in various industries, such as medicine, aerospace, and food processing (Li, W. et al., 2025). Three-dimensional food printing (3DFP) enables the production of complex and customized food structures that are difficult to achieve through conventional methods (Yang et al., 2017). Also, 3DFP supports personalized food production by enabling the use of diverse ingredients and the development of health-oriented meals tailored to individual dietary needs (Lee, 2021; Wu et al., 2024).

Due to the inherently complex system of food, 3DFP often encounters difficulties in meeting printability standards, resulting in challenges such as poor product shaping, reduced structural stability, low printing precision, and decreased efficiency (Cao et al., 2022; Tian et al., 2021). The printability of a material determines its suitability for 3DFP and refers to its ability to be smoothly and continuously extruded through a nozzle under specific force while retaining its shape after extrusion, supporting its weight throughout the printing process, and maintaining structural stability without deformation once printing is complete (Cao et al., 2022; Outrequin et al., 2023). Since the rheological properties of food inks are critical determinants of printability, research has focused on characterizing these properties and optimizing formulations to enhance printability (Cao et al., 2022; Ma et al., 2023).

Conventional methods for evaluating printability in relation to the physicochemical and rheological properties include the analysis of water holding capacity (WHC), texture and gel strength, and microstructural analysis using scanning electron microscopy (Lu et al., 2024; Wei et al., 2024). While these methods provide reliable and precise assessments of 3DFP printability, they have several limitations. They

* Corresponding author. Department of Convergence Biosystems Engineering, Chonnam National University, Gwangju, 61186, Republic of Korea.
** Corresponding author. Department of Integrative Food, Bioscience and Biotechnology, Chonnam National University, Gwangju 61186, Republic of Korea.
E-mail addresses: hison@jnu.ac.kr (H.I. Son), bioksj@jnu.ac.kr (S.-J. Kim).

https://doi.org/10.1016/j.jfoodeng.2025.112725
Received 24 May 2025; Received in revised form 28 June 2025; Accepted 1 July 2025
Available online 2 July 2025

require significant time and resources with specialized equipment and skilled personnel. Also, they often involve additional steps such as point-by-point analysis or destructive sample homogenization. These constraints make them unsuitable for automation and limit the reuse of processed samples (Mutlu et al., 2011; Yam and Papadakis, 2004). Consequently, there is a clear need to develop more efficient, automated approaches for assessing the printability and quality of 3DFP products.

Recently, advanced technologies such as machine learning, deep learning, and computer vision (CV) have been adopted in the evaluation of automated printability in 3D printing. These technologies have been applied to a variety of cases, including the prediction of the printability of biomaterials, the prediction of processability and fabrication conditions for pharmaceutical formulations, and the evaluation of the printability of concrete-based materials (Elbadawi et al., 2020; Liu, C. et al., 2022; Marcucci et al., 2023). Among these technologies, CV, an interdisciplinary field integrating informatics, mathematics, and image processing, enables computers to analyze and interpret visual information such as images and video (Paraskevoudis et al., 2020). In particular, CV has gained increasing recognition as a core technology for quality assessment and process optimization in 3D printing. CV-based systems have been effectively utilized to monitor print quality in real time and to detect and correct errors occurring during the printing process (Paraskevoudis et al., 2020). Moreover, hardware and software frameworks that incorporate layer-wise analysis, defect detection, and automatic correction functions have also been proposed (Petsiuk and Pearce, 2020).

Research has also actively explored precise control of the extrusion characteristics of food inks in 3DFP. For example, researchers have utilized machine learning to measure the instantaneous extrusion rate and filament width under constant pressure or force and implemented feedforward control of nozzle movement in pneumatic 3D food printers (Ma et al., 2023). A recent study integrated image analysis with machine learning, demonstrating that the printability of polysaccharide-based food inks could be accurately predicted based on their composition and rheological properties, thereby significantly expanding the potential for automation in food manufacturing processes (Lu et al., 2023).

Despite these technological advances, studies evaluating the printability of food materials using image-based features remain remarkably limited in their scope, often focusing on extrusion parameters or general material properties. Crucially, research directly linking the quantitative analysis of visual texture features from printed structures of protein-based food inks to critical functional attributes like WHC and gel strength is notably scarce. This study proposes a proactive methodology: rather than merely detecting post-print defects, we leverage sophisticated digital image analysis to predict printability outcomes and structural quality before widespread issues arise, thereby enabling real-time optimization and overcoming the inherent limitations of conventional, reactive assessment methods.

To establish CV-based printability evaluation, we employed a sophisticated methodology that goes beyond simple image analysis. Quantitative visual texture features, extracted meticulously from digital images of printed structures, were combined with additive concentration data. This rich, multi-faceted dataset was then used to train a Random Forest (RF) model. This approach enabled the simultaneous and precise prediction of critical printability indices like WHC and gel strength, thereby revealing a nuanced quantitative relationship between additive composition and printing performance. Unlike conventional, labor-intensive, and often destructive physical measurements, our data-driven model offers exceptional efficiency and accuracy, providing a superior tool for optimizing 3DFP processes. Furthermore, to enhance the model's transparency and provide visual insights into how texture features influenced the model's predictions, Shapley Additive Explanations (SHAP) analysis was conducted.

Surimi was selected as the foundational model material for this methodology, as it is a stabilized concentrate of myofibrillar proteins, characterized by its high protein and low-fat content. It is produced by washing and dehydrating deboned fish meat and is widely used as a key raw material in various processed seafood products such as fish cakes and fish sausages (Kim et al., 2022; Li et al., 2023). However, with growing consumer demand for enhanced nutritional value and customized product appearance, conventional surimi products face limitations in achieving personalized shapes and functional attributes. To overcome these challenges, 3D food printing has emerged as a promising alternative. Due to its homogeneous and highly viscous gel-forming properties, surimi demonstrates excellent structural support after extrusion, making it a suitable material for 3D food printing applications (Dong et al., 2020). Nevertheless, its physicochemical properties are highly sensitive to factors such as WHC and hydrogen bonding interactions, which can significantly affect printing performance (Li et al., 2023). Considering surimi's intricate properties and the limitations of conventional evaluation methods, there's a growing need for a non-destructive, quantitative, and efficient approach to assess the printability of protein-based food inks.

In this study, we developed a CV-based regression model to predict the WHC and gel strength of printed surimi ink, providing an efficient and automation-compatible alternative to conventional evaluation methods (Fig. 1). Specifically, we first investigated the printability of surimi as influenced by the addition of NaCl and TGase. Second, we analyzed the WHC and gel strength of surimi ink using conventional methods. Finally, we applied texture features extracted from digital images, along with additive concentration data, to an RF model for the simultaneous prediction of WHC and gel strength, thereby revealing the quantitative relationship between additive composition and printability indices.

2. Materials and method

2.1. Materials

For surimi, frozen *Scomberomorus niphonius* fillets were purchased from Garyon Seafood Co., Ltd. (Busan, South Korea) and stored at −18 °C. Sodium chloride (NaCl) and transglutaminase (TGase), used as additives in surimi ink, were obtained from CJ Corp. (Incheon, South Korea) and Ajinomoto Co., Inc. (Tokyo, Japan), respectively.

2.2. 3DPF of surimi ink

To prepare surimi ink, the frozen fillets were thawed in water for 30 min and then rinsed, dried, trimmed, and minced using a blender (HR2041/01, Philips, Netherlands) for 1 min. NaCl was incorporated at concentrations ranging from 0.5–4 % (*w/w*) of the surimi weight, followed by the addition of ice water at 15 % (*w/w*). The samples were then mixed with TGase at concentrations ranging from 0.1–0.4 % (*w/w*), also based on the surimi weight. After blending the surimi mixture for 3 min, it was transferred into a plastic extruder tube.

For 3DFP, a SMART3D FoodBot (Oseong System Co., Ltd., South Korea) was used. Fig. 2 illustrates the hardware setup of the 3D printer employed in this study. A star-shaped model (60 × 60 × 12 mm^3) was designed in Tinkercad (Autodesk Inc., San Rafael, CA, USA) and saved as an STL file for slicing. The slicing was performed using Slic3r software, which generated a G-code specifying material deposition paths and printing parameters. This G-code was then uploaded to the printer via Repetier-Host (version 4.0.1, Hot-World GmbH & Co. KG, Willich, Germany), enabling precise control of nozzle movement, deposition speeds, and extrusion rates, ensuring reliable printing results. All experiments were conducted at room temperature, and the optimized printing conditions, determined through preliminary trials, are provided in Table 1.

2.3. Analysis of water holding capacity (WHC)

For WHC analysis, the 3D-printed surimi required post-processing,

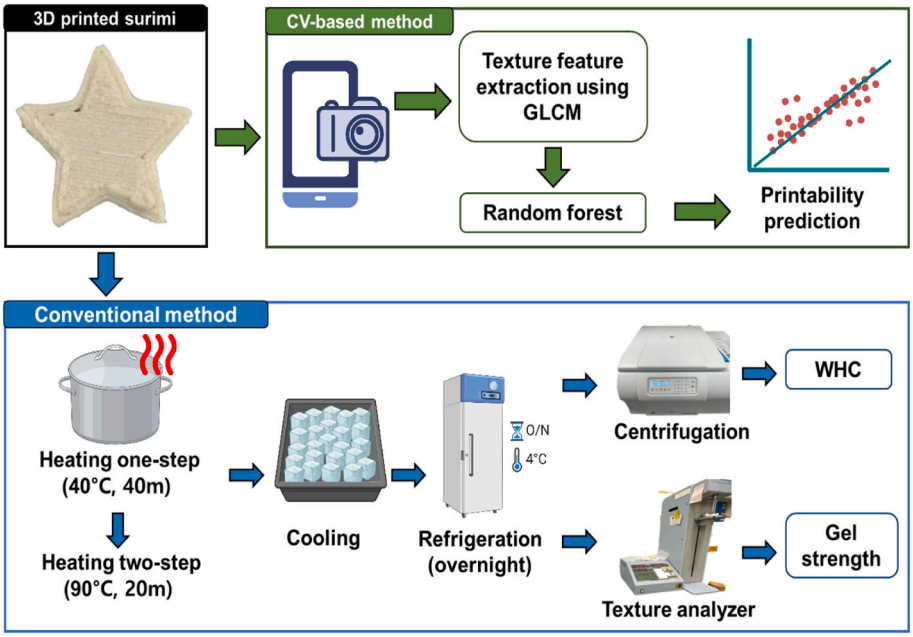

Fig. 1. Overview of printability measurement in 3DFP.

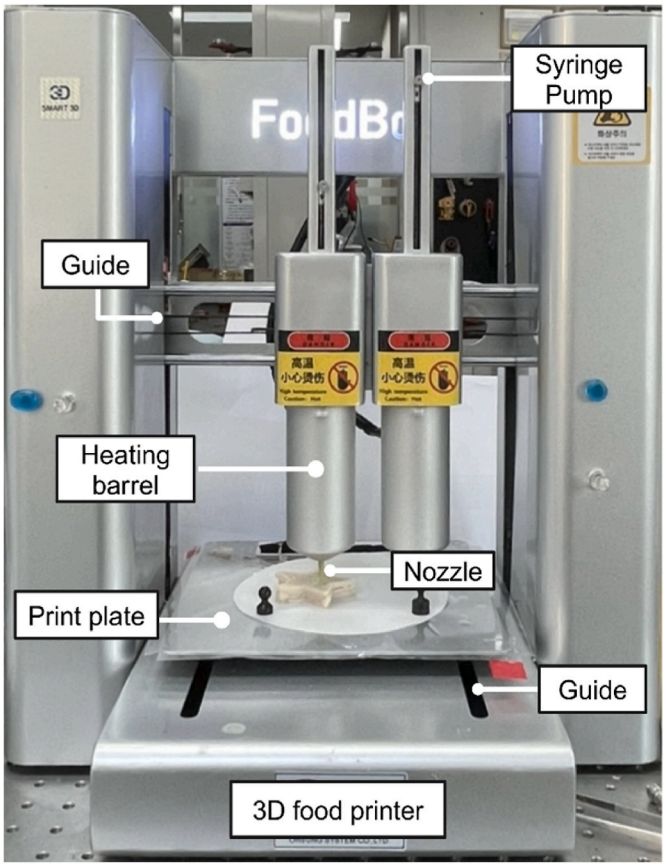

Fig. 2. Hardware configuration: Syringe pump controls material flow for consistent extrusion; Heating barrel maintains optimal temperature for smooth extrusion; Print plate provides a heated base for proper material adhesion; Nozzle ensures accurate extrusion, affecting print quality and speed.

including heating and cooling (Fig. 1). Samples were heated in a pre-heated water bath at 40 °C for 40 min, then further heated at 90 °C for 20 min. After cooking, the surimi gel was rapidly cooled on ice and

Table 1
3D extrusion printing parameters.

Parameter	Value
Nozzle diameter	1.5 mm
Layer height	2.0 mm
Infill density	80 %
Infill pattern	Linear
Nozzle speed	15 mm/s

refrigerated overnight at 4 °C prior to analysis. The WHC of surimi was evaluated using a previously reported method with some modifications (Cao et al., 2022). A 4.0 g sample was excised from the center of the post-processed surimi, wrapped in filter paper, and placed into a 50 mL conical centrifuge tube lined with several layers of blotting paper at the bottom. The samples were centrifuged at 4000 rpm for 10 min at 4 °C using a centrifuge (1580R, Labogene Co., Ltd., Korea). After centrifugation, the supernatant was removed, and the sample weight was measured. WHC was determined by calculating the percentage of water removed from the sample during centrifugation, relative to its initial weight, which was obtained by weighing the supernatant. WHC is defined by Eq. (1):

$$WHC(\%) = 100 \times \left(\frac{m_2}{m_1}\right) \quad (1)$$

where m_1 represents the weight of the sample before centrifugation, and m_2 denotes the weight of the sample after centrifugation.

2.4. Analysis of gel strength

The gel strength of the post-processed sample was evaluated at room temperature using a texture analyzer (CR-500DX-L, SUN SCIENTIFIC CO., LTD, Tokyo, Japan). Following extensive preliminary experiments, a deformation speed of 2 mm/s was applied during both the pre-test and post-test phases. The 3D-printed samples exhibited considerable variability in surface characteristics and internal infill structures due to differing concentrations of salt and transglutaminase. Consequently, these structural heterogeneities often led to uneven resistance during probe penetration. For instance, when the probe speed was too slow, it tended to dwell on structurally weak regions, resulting in excessive

deformation and increased measurement variability. Conversely, higher speeds limited adequate contact between the probe and sample surface, compromising measurement accuracy. Therefore, among the tested conditions, a speed of 2 mm/s consistently yielded the most stable and reproducible results across all samples. The breaking force (N) and penetration distance (mm) were measured using a cylindrical probe with a 5 mm diameter. The trigger mode was set to automatic, and each test was conducted in triplicate to ensure consistency. Gel strength was calculated as shown in Eq. (2):

$$G_{strength} = F_{breaking} \cdot D_{deformation} \tag{2}$$

where $F_{breaking}$ indicates the breaking force, $D_{deformation}$ denotes the deformation, and $G_{strength}$ represents the gel strength.

2.5. Establishment and evaluation of a predictive model for printability

Fig. 3 illustrates the framework for quantitative modeling of 3DFP printability. Surface texture features are extracted through image processing, were combined with salt and TGase concentrations as inputs for the RF model. This model predicts WHC and gel strength. The performance of the Top view (TOP model), Side view (SIDE model), and the combined TS model were compared to identify the optimal predictive model.

2.5.1. Image acquisition and processing

All image processing algorithms were developed and implemented in Python 3.8.10 to evaluate the surface characteristics of 3D printed surimi samples. Images were acquired using an iPhone 12 at a resolution of 2532 × 1170 pixels, with the samples placed on white parchment paper to ensure a standardized and uniform background. For the top-view images, the camera lens was positioned approximately 12 cm above the sample surface and oriented perpendicularly. For the side view images, the lens was aligned orthogonally to the sample's side at a distance of approximately 10 cm. To maintain data reliability and consistency, samples affected by printing interruptions, such as nozzle clogging or ink shortages, were excluded from the imaging procedure.

The captured RGB images were converted to grayscale to facilitate texture analysis. Denoising techniques were applied to minimize noise while preserving structural details and edges. To improve texture features and contrast, an adaptive mean adjustment method was employed by dividing the image into 3 × 3 non-overlapping blocks and normalizing the pixel values within each block. Additionally, Gaussian smoothing was applied to enhance texture uniformity and highlight local variations.

The region of interest (ROI) was precisely delineated by applying Otsu thresholding to the binary image, followed by contour extraction. This approach ensured that the analysis focused solely on the relevant surface of the sample, effectively excluding the background regions. Subsequently, gray level co-occurrence matrix (GLCM) analysis was performed to quantify texture features such as contrast and correlation, which were then used to assess key surface properties.

2.5.2. Extraction of texture feature using GLCM

The GLCM is a widely used method for analyzing and quantifying texture in images (Haralick et al., 1973). It determines the frequency of specific gray-level intensity pairs occurring in a defined spatial relationship, characterized by both distance and direction, thereby capturing the spatial properties of the texture. Represented as a symmetric square matrix, each element in the GLCM corresponds to the co-occurrence frequency of gray-level pairs between a reference pixel and its neighboring pixel. The computed co-occurrence frequencies are then normalized to probabilities, as expressed in Eq. (3):

$$P(i,j) = \frac{N_{ij}}{\sum_{i=0}^{m-1}\sum_{j=0}^{m-1} N_{ij}} \tag{3}$$

where $P(i,j)$ represents the probability that the reference pixel and its neighboring pixel have gray levels i and j, respectively, N_{ij} denotes the number of co-occurrences where the gray levels are i and j, and $\sum_{i=0}^{m-1}\sum_{j=0}^{m-1} N_{ij}$ represents the total number of co-occurrences in the GLCM.

GLCM enables the extraction of critical texture features, including Contrast, Correlation, Entropy, Homogeneity, and Energy, which quantitatively describe texture characteristics. In this study, the GLCM was constructed locally for each window within the ROI to capture localized texture variations. Texture feature extraction was automated using a Python-based algorithm developed specifically for this purpose, ensuring precise and efficient analysis of the image data. To prevent certain features from dominating the classifier due to their scale, all features were standardized during the training process.

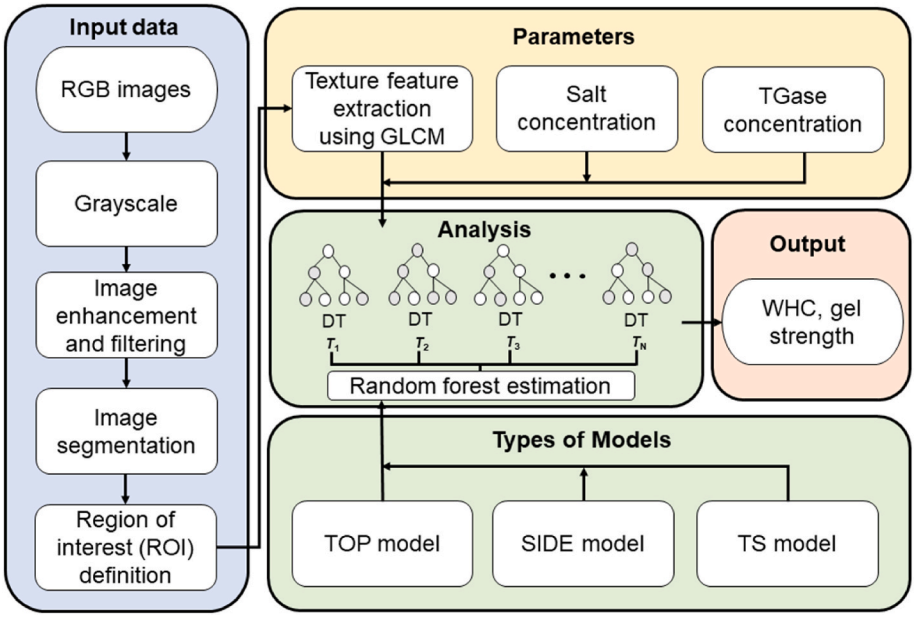

Fig. 3. Quantification modeling framework for printability in 3DFP.

Contrast represents the local variation in texture. Higher values indicate greater texture variation, which is calculated by squaring the difference in gray levels between the reference pixel and its neighboring pixels. It is mathematically represented as follows:

$$Contrast = \sum_{i=0}^{m-1}\sum_{j=0}^{m-1}(|i-j|)^2 P(i,j) \tag{4}$$

where $|i-j|^2$ represents the squared difference between the grayscale value of the reference pixel i and that of the neighboring pixel j, assigning greater weights to larger differences. m denotes the total number of grayscale levels utilized in the image.

Correlation describes the linear relationship in the texture. It measures how similar the texture is in horizontal and vertical directions. It can be defined mathematically as follows:

$$Correlation = \frac{\sum_{i=0}^{m-1}\sum_{j=0}^{m-1}(i-\mu_i)\left(j-\mu_j\right)P(i,j)}{\sigma_i \cdot \sigma_j} \tag{5}$$

where $(i-\mu_i)$ and $\left(i-\mu_j\right)$ represent the deviations of the grayscale values i and j from their respective means μ_i and μ_j quantifying the linear dependence between pixel intensities. The terms μ_i and μ_j denote the mean grayscale values of the reference and neighboring pixels, respectively, while σ_i and σ_j are their corresponding standard deviations, measuring the variability in grayscale values. The product $\sigma_i \cdot \sigma_j$ serves as a normalization factor, ensuring that the correlation is dimensionless and constrained within the range $[-1, 1]$.

Entropy quantifies the complexity of the texture's information. Higher entropy values indicate greater uncertainty and diversity in the texture. It is formulated mathematically as follows:

$$Entropy = -\sum_i\sum_j P(i,j)\cdot\log(P(i,j)+\varepsilon) \tag{6}$$

where $log(P(i,j)+\varepsilon)$ represents the logarithm of $P(i,j)$, with a small constant ε introduced to prevent undefined values when $P(i,j)=0$. This modification ensures numerical stability during computation. $\sum_i\sum_j$ denotes the summation over all possible grayscale levels i and j in the GLCM. This ensures that all pixel pair occurrences in the texture are considered when calculating entropy.

Energy measures the uniformity of the texture, with higher values indicating a more homogeneous pattern. It is mathematically defined as follows:

$$Energy = \sum_{i=0}^{m-1}\sum_{j=0}^{m-1}P(i,j)^2 \tag{7}$$

Homogeneity, also known as Inverse Difference Moment, quantifies the closeness of gray levels within the texture. It is calculated as:

$$Homogeneity = \sum_{i=0}^{m-1}\sum_{j=0}^{m-1}\frac{P(i,j)}{1+|i-j|} \tag{8}$$

2.5.3. Training of CV-based model using machine learning

The RF algorithm, implemented using Python 3.8.10, was integrated with CV-based image processing to predict the printability of 3D-printed surimi samples. RF was chosen for its robustness and versatility in handling high-dimensional data and noisy features. As an ensemble learning model, RF aggregates multiple decision trees to map input data to output values. It is widely applied to regression problems, where the output is a continuous value, and classification problems, where the output is a discrete class. By averaging predictions (for regression) or voting (for classification), RF enhances both predictive accuracy and generalization performance (Breda et al., 2024). A key advantage of RF is its ability to assess the relative importance of input variables, enabling quantitative analysis of their contributions. Its embedded bagging mechanism generates multiple bootstrap samples and combines predictions, thereby reducing overfitting while maintaining model stability (Fukuda et al., 2014).

2.5.4. Printability modeling

To address the issue of multicollinearity, Variance Inflation Factor (VIF) analysis was conducted. The input variables included TGase concentration, salt concentration, and GLCM-based surface texture features extracted from the images. Variables with VIF values exceeding 10.0 were removed to enhance model robustness. The refined dataset was then used to predict printability-related parameters, such as WHC and gel strength. The input variables for the RF model consisted of TGase concentration, salt concentration, and five GLCM-based surface texture features—Contrast, Correlation, Entropy, Homogeneity, and Energy.

The dataset was collected from three different perspectives: top view, side view, and a combination of both (Top view + Side view, TS model). Based on these perspectives, three RF models were developed and designated as the TOP, SIDE, and TS models, respectively. RF computations employed bootstrap resampling to construct multiple decision trees, while variable importance was assessed based on mean squared error (MSE) reduction. Specifically, the importance of each variable was determined by aggregating the MSE reductions from all splits involving that variable across all decision trees.

2.5.5. Model evaluation

To evaluate the performance of the printability prediction model, the Mean Absolute Error (MAE), Coefficient of Determination (R^2), and Root Mean Square Error (RMSE) were used as the primary evaluation metrics. A lower MAE and RMSE values, as well as an R^2 value closer to 1, indicate higher prediction accuracy. These metrics are calculated using the following equations:

$$MAE = \frac{1}{N}\sum_{i=1}^{N}|y_i-\hat{y}_i| \tag{9}$$

$$R^2 = 1-\frac{\sum_{i=1}^{N}(y_i-\hat{y}_i)^2}{\sum_{i=1}^{N}(y_i-\bar{y})^2} \tag{10}$$

$$RMSE = \sqrt{\frac{1}{N}\sum_{i=1}^{N}(y_i-\hat{y}_i)^2} \tag{11}$$

here, y_i represents the observed value, $\hat{y}_i$ is the predicted value, $\bar{y}$ indicates the mean of the observed values, and N denotes the number of samples in the dataset.

2.5.6. Model interpretation with the SHAP method

In this study, the SHAP (Shapley Additive Explanations) method (Lundberg and Lee, 2017a) was introduced to complement the interpretation of a regression-based RF model developed to predict physical properties—namely, WHC and gel strength—of 3D-printed surimi samples. SHAP offers an interpretable framework by computing Shapley values, which quantify the extent to which each input feature contributes to the predicted continuous outcome. The Random Forest model provides a global assessment of feature importance by averaging reductions in MSE across all decision trees. These global importance scores are helpful in identifying features that contribute most, on average, to model performance across the entire dataset. However, they do not capture how individual features affect specific predictions. In this context, SHAP was additionally employed to address this limitation and to enable instance-level interpretability.

SHAP is grounded in cooperative game theory (Lundberg and Lee, 2017b), wherein the marginal contribution of each feature is calculated by comparing model outputs with and without the feature across all

possible feature subsets. This is formalized using an additive linear model:

$$g(z') = \phi_0 + \sum_{i=1}^{M} \phi_i z_i' \quad (12)$$

where ϕ_i denotes the Shapley value, z_i indicates the presence of the feature, and M represents the total number of input variables.

In this study, SHAP values were computed based on a RF model trained with GLCM-derived texture features, and the implementation was carried out using the Python SHAP package. The resulting SHAP values were visually mapped onto both top and side view images to identify the local regions that contributed most significantly to the prediction of WHC and gel strength.

2.6. Statistical analysis

All experiments were conducted in triplicate, and the results were expressed as mean ± standard deviation. Statistical analysis was performed using R software (version 4.4.1), applying one-way analysis of variance (ANOVA) followed by Duncan's multiple range test. Differences were considered statistically significant at $p < 0.05$.

3. Results and discussion

3.1. Investigation of the printability performance of surimi with the addition of NaCl and TGase

Since the addition of NaCl and TGase has been reported to affect the 3D printability in surimi-based 3DFP, various concentrations of NaCl (0.5–4 %) and TGase (0–0.4 %) were incorporated into surimi ink to evaluate its printability performance. When only 0.5 % NaCl was added

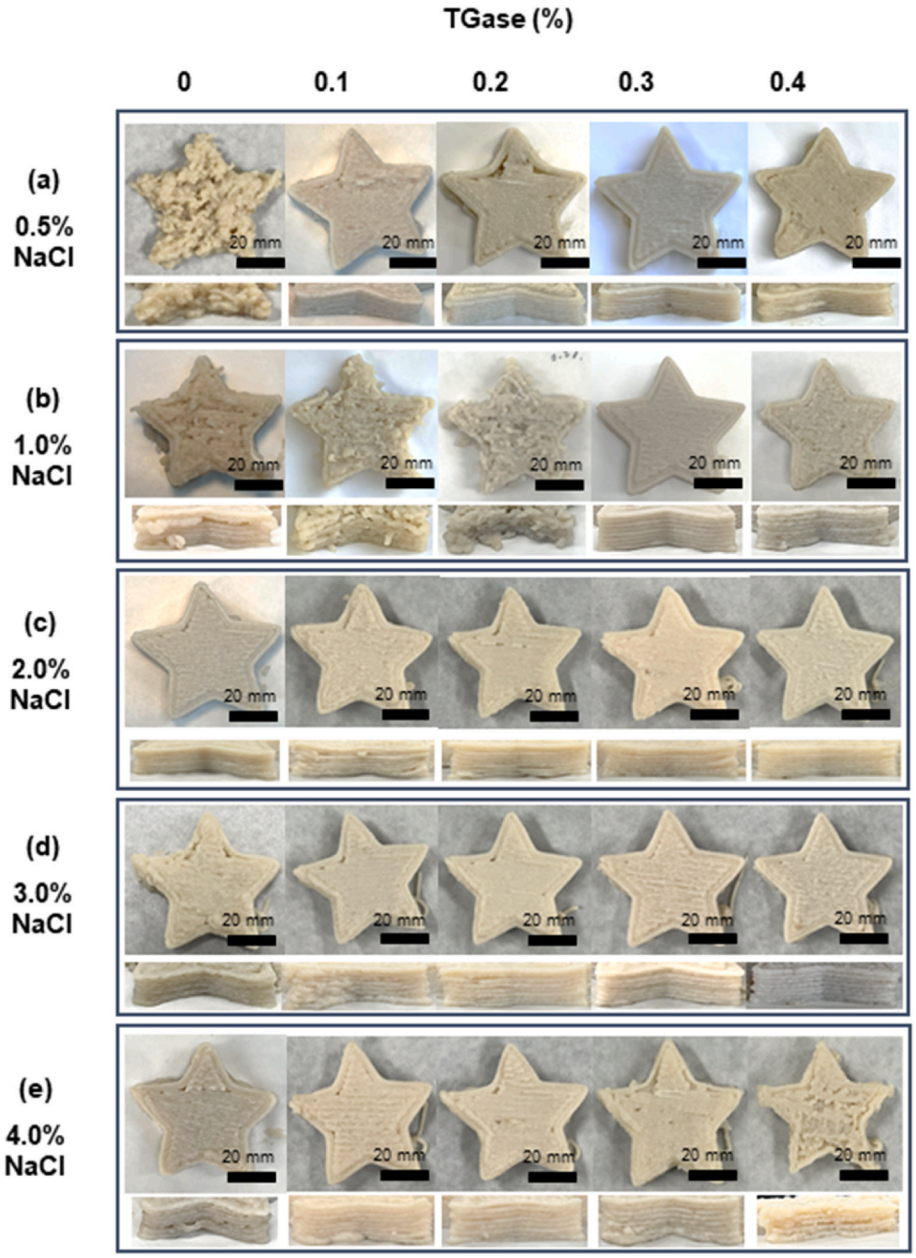

Fig. 4. Printing quality of surimi gels under varying NaCl and TGase concentrations. (a–e) Actual printed structures at different NaCl concentrations (a = 0.5 %, b = 1.0 %, c = 2.0 %, d = 3.0 %, e = 4.0 %), each with TGase levels ranging from 0 % to 0.4 % (w/w).

without TGase, the printed surimi exhibited extremely low structural stability, tending to collapse and failing to maintain its shape (Fig. 4a). In contrast, the addition of 1 % or more NaCl enabled the printed surimi to retain its basic shape even in the absence of TGase, with a general improvement in structural integrity observed (Fig. 4b–e). This trend aligns with previous research by Cao et al. (2022), which demonstrated that low NaCl content increased storage modulus and hindered extrusion, whereas excessive NaCl reduced printing precision. Both findings are consistent with the observations made in the present study.

While extrusion irregularities and poor interlayer adhesion were observed across most NaCl concentrations when TGase was absent, the addition of TGase led to denser printed structures with smoother surfaces and fewer cracks. This improvement appears to be due to covalent cross-linking between myosin molecules induced by TGase, which reinforces the protein network and enhances the structural stability of printed constructs (Yu et al., 2022). Although the addition of TGase contributes to improving the printability of surimi, adding 0.4 % TGase can cause inconsistent and rough surfaces of printed products. This adverse effect was most pronounced under the 4 % NaCl and 0.4 % TGase condition (Fig. 4e). These findings are consistent with previous reports indicating that MTGase concentrations of 0.2 % and 0.3 % yield optimal printed structures, whereas concentrations exceeding 0.4 % result in a loss of extrusion uniformity and print consistency (Dong et al., 2020).

In this study, more than 1 % NaCl or at least 0.1 % TGase was required to ensure post-printing stability, showing improved shape retention and internal pattern fidelity, closely matching the 3D printing model. Notably, the printed surimi exhibited the most favorable printability, maintaining smooth and stable external appearances when 0.5 % or 1 % NaCl with 0.3 % TGase and 2 % NaCl with no TGase were added to the surimi ink (Fig. 4a–c). Subsequently, surimi samples with various printability were used to evaluate WHC and gel strength.

3.2. Analysis of WHC and gel strength to evaluate printability of surimi ink

Among the various parameters used to assess the quality of food gels, WHC and gel strength are widely recognized as key indicators, as they

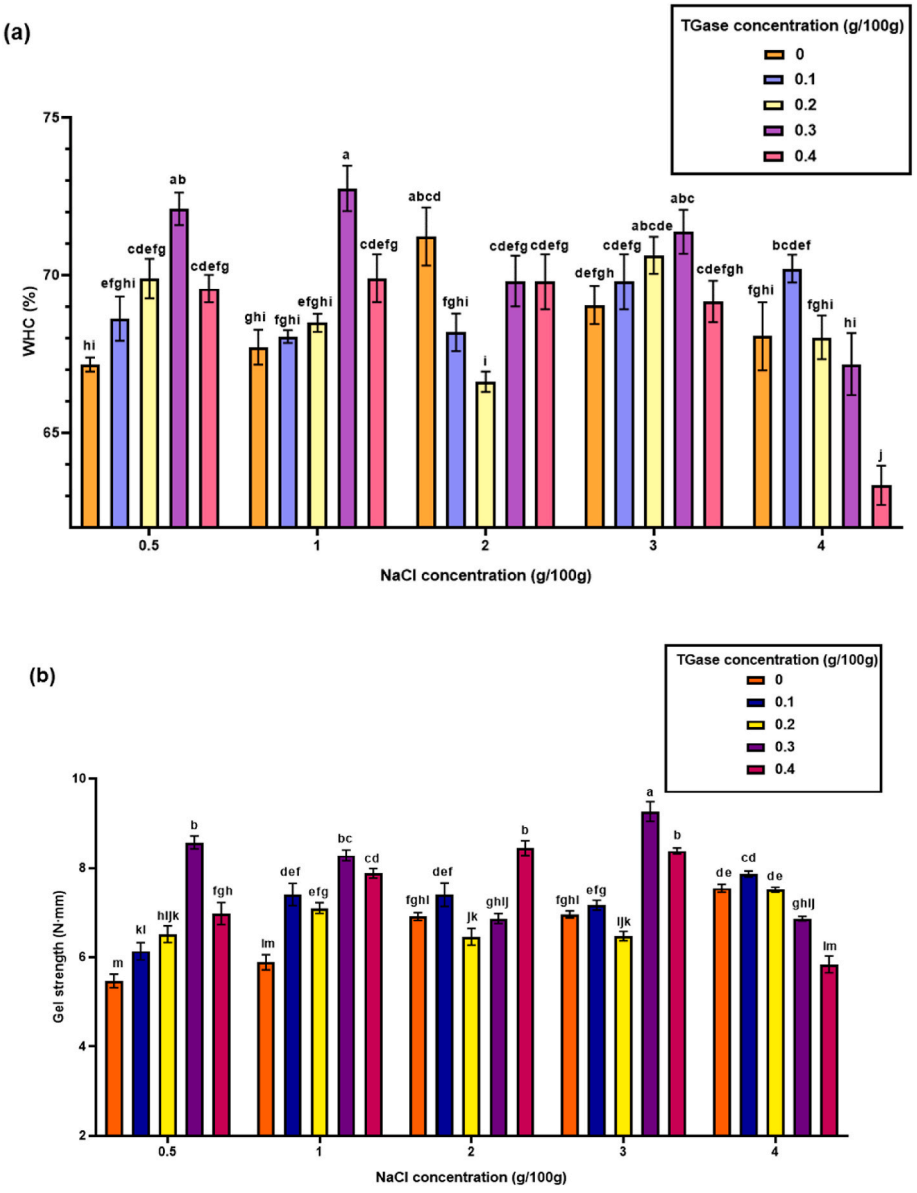

Fig. 5. WHC (a) and gel strength (b) of 3D-printed surimi gels formulated with five levels of NaCl (0.5 %, 1 %, 2 %, 3 %, and 4 %) and corresponding TGase concentrations (0 %, 0.1 %, 0.2 %, 0.3 %, and 0.4 % w/w).

objectively reflect the physical properties and overall quality of printed structures (Li, H. et al., 2025a). Previous studies have also examined the relationships among WHC, rheological properties, and printability within surimi–starch systems. In particular, cluster analysis revealed that starch type and concentration, WHC, and rheological behavior are strongly associated with 3D printability (Liu, Y. et al., 2022). Accordingly, this study analyzed WHC and gel strength of surimi samples with various printability levels for evaluating the quality and physical properties of the printed structure.

As shown in Fig. 5a, the WHC exhibited a statistically significant increase with increasing NaCl concentration ($p < 0.05$). This finding is consistent with previous studies. For instance, Cao et al. (2022) reported that higher NaCl levels enhance the water-holding capacity of surimi gels by reducing water mobility and reinforcing the overall gel network structure. Similarly, Wang et al. (2018) demonstrated that WHC significantly increases with NaCl addition, attributing this effect to the binding of chloride ions to myofibrillar proteins, which elevates electrostatic repulsion between filaments and consequently enhances the affinity of proteins for water.

In most NaCl concentration conditions, the addition of TGase significantly increased the WHC ($p < 0.05$), suggesting that TGase enhances water-holding capacity by promoting the formation of a more stable and compact three-dimensional gel network (Yu et al., 2022). Additionally, Cando et al. (2016) reported that TGase facilitates protein cross-linking, leading to the formation of a looser protein matrix capable of entrapping more water, thereby improving the WHC of low-salt surimi.

Meanwhile, under the condition of 2 % NaCl, the highest WHC was observed in the absence of TGase. This may be attributed to the ability of NaCl alone to enhance the swelling of myofibrillar proteins through chloride ion binding, which increases electrostatic repulsion between filaments and, in turn, improves the water affinity of proteins, resulting in a more stabilized water-retaining network (Wang et al., 2018).

Surimi gels prepared with 1 % NaCl and 0.3 % TGase, 0.5 % NaCl and 0.3 % TGase, and 2 % NaCl without TGase exhibited high WHC. These samples also demonstrated smooth extrusion through the nozzle during printing, along with high layer-stacking precision and overall print quality. These findings suggest that high WHC contributes to improved structural stability and surface uniformity, indicating a close association between WHC and printability in surimi-based systems. In contrast, although the samples prepared with 3 % NaCl and 0.3 % TGase, and 4 % NaCl and 0.2 % TGase also showed high WHC values, surface pores were observed in the printed constructs. This indicates that the relationship between WHC and printing performance is not strictly linear. In particular, at higher concentrations of NaCl and TGase, elevated WHC does not necessarily translate into optimal print quality. A similar phenomenon was also observed in the study by Cao et al. (2022).

Gel strength is a key indicator for assessing the mechanical properties of surimi gels and is closely associated with the structural stability of the final product as well as its printing properties (Sun et al., 2025). Accordingly, gel strength plays a critical factor in determining the self-supporting capability of 3D-printed structures and directly influences the printability of surimi-based materials (Dong et al., 2019).

As shown in Fig. 5b, even in the absence of TGase, gel strength progressively increased with higher concentrations of NaCl. This trend is consistent with the findings reported by Cao et al. (2022) and Wang et al. (2018), both of which demonstrated a significant enhancement in the gel strength of surimi with increasing NaCl content. Notably, the gel strength profile observed in the NaCl-only groups in the present study closely resembled that reported by Cao et al. (2022). The increase in gel strength can be attributed to the swelling of myofibrillar proteins, which enhances intermolecular interactions among protein molecules, an effect promoted by the presence of NaCl (Cao et al., 2022; Wang et al., 2018). Such enhancement in gel strength effectively supported the self-weight of the printed structures during the 3D printing process and contributed to the maintenance of stable three-dimensional forms thereafter.

In most NaCl conditions, the incorporation of TGase significantly enhanced gel strength ($p < 0.05$), presumably through the formation of ε-(γ-glutamyl) lysine bonds between myosin and actomyosin (Yu et al., 2022). These covalent cross-links reinforced the protein network and facilitated the development of a more robust three-dimensional gel structure. However, under the condition of 4 % NaCl, a paradoxical decrease in gel strength was observed despite higher TGase concentrations. This may be due to excessive isopeptide bond formation, which can hinder protein–water interactions, induce water loss, and ultimately result in an overly rigid yet brittle gel network (Dong et al., 2020; Wang et al., 2018). Moreover, the disruption of protein-water interactions due to excessive isopeptide bond formation not only compromised the gel's ability to retain structural integrity but also led to increased water loss, resulting in a reduction in WHC. Therefore, the observed paradoxical decreases in both gel strength and WHC under high NaCl and TGase concentrations can be attributed to these combined effects.

Surimi gels prepared under the conditions of 3 % NaCl with 0.3 % TGase and 1 % NaCl with 0.3 % TGase exhibited high gel strength along with overall favorable print quality. In contrast, samples formulated with 2 % NaCl and 0.4 % TGase, 3 % NaCl and 0.4 % TGase, and 1 % NaCl and 0.4 % TGase demonstrated reduced surface quality despite their elevated gel strength. A similar trend was observed in the study by Cao et al. (2022), where low gel strength resulted in poor printability, while excessive gel strength also led to surface defects such as pore formation, thereby diminishing print quality. Likewise, visual patterns reported by Yu et al. (2022) indicated that under high gel strength conditions, the surfaces of printed samples often appeared uneven and rough, with such irregularities particularly appearing on the side surfaces. However, in the present study, although some high–gel strength conditions exhibited slightly diminished surface quality, the side-view images of the printed samples revealed relatively precise layer stacking, suggesting that vertical structural integrity was well maintained.

3.3. Quantification of printability in 3D printed surimi samples

Images of all 75 3D-printed surimi samples were acquired and converted to grayscale. A series of image preprocessing steps were then applied to define the ROI for each sample. Texture features based on the GLCM were extracted from each ROI, and the values were normalized to ensure consistency across the dataset. All samples were included in the analysis, while representative top view (Fig. 6a) and side view (Fig. 6b) images under selected conditions are presented in Fig. 6 to illustrate typical surface variations.

To quantitatively predict WHC and gel strength, three RF models — the TOP, SIDE, and TS models — were developed using GLCM features and additive concentrations as input variables. The dataset was split into training (70 %) and test (30 %) subsets to ensure reliable model evaluation and prevent overfitting.

The results are summarized in Table 2. The TOP model demonstrated the highest predictive accuracy for WHC in RF modeling. In the training set, it achieved a MAE of 0.510, an R^2 of 0.907, and an RMSE of 0.714, while in the test set, it yielded a MAE of 0.674, an R^2 of 0.875, and an RMSE of 0.831 (Fig. 7a). These results indicate that top-view surface images effectively capture the relationship with WHC, offering excellent predictive performance.

In contrast, both the SIDE model and the TS model failed to capture sufficient information related to WHC, resulting in relatively lower prediction accuracy. This outcome can be attributed to the inherent characteristics of WHC, which is highly dependent on the gel matrix's ability to retain water. Surimi samples with high WHC tend to exhibit smoother and glossier surfaces due to the formation of dense and hydrated gel networks. These visual traits—such as surface flatness, luster, and fine crack distribution—are more prominently visible in top-view images. Conversely, side views primarily reflect layer-wise stacking and interfacial adhesion, which are less indicative of water retention

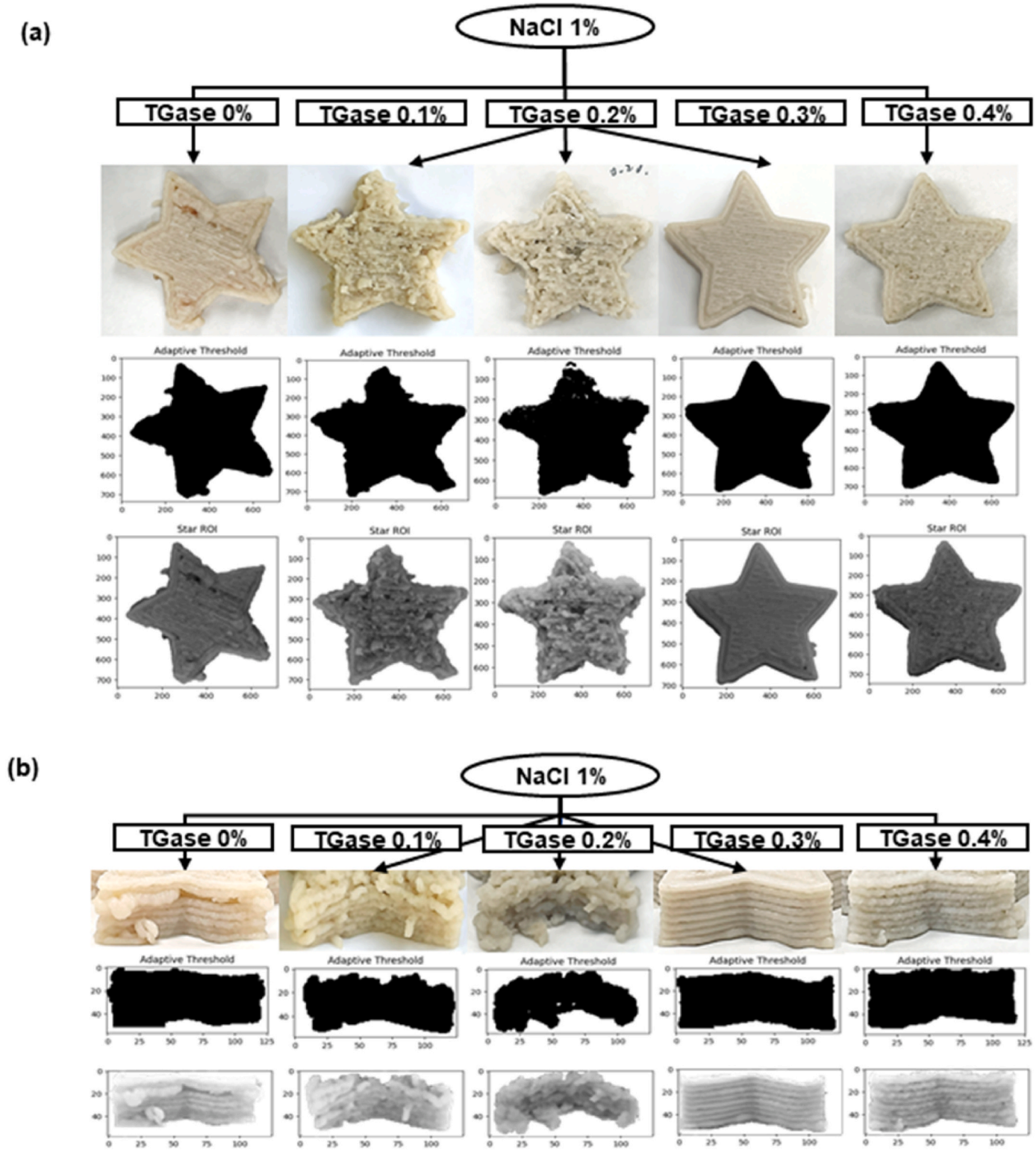

Fig. 6. Images from the top and side views. (a)Top view images of samples exhibiting the most pronounced surface changes under the 1 % NaCl condition with varying TGase concentrations (0–0.4 %) are presented. These images were converted to grayscale and underwent a series of preprocessing steps to define the ROI for each sample, (b) Corresponding side view images under the same conditions are also provided to visually illustrate representative surface variations.

properties. Therefore, top-view imaging provides a more informative representation of surface conditions directly linked to WHC-related structural properties, offering more relevant visual cues for accurate prediction.

For gel strength, the TS model achieved a MAE of 0.460, an R^2 = 0.744, and an RMSE of 0.672 on the training set (Fig. 7b). On the test set, it recorded a MAE of 0.391, an R^2 = 0.691, and an RMSE of 0.556 (Fig. 7b), where the figure depicts a graph comparing the predicted and actual values. Notably, the TS model exhibited the lowest prediction errors in terms of MAE and RMSE during testing, indicating strong predictive performance. In contrast, while the SIDE model demonstrated superior performance during training, it exhibited increased errors on

Table 2
Performance comparison of the TOP, SIDE, and TS models in predicting printability (WHC and gel strength) of 3D-printed samples during training and testing.

Printability	Model	Metrics	Train	Test
WHC	TOP	MAE	0.510	0.674
		R^2	0.907	0.875
		RMSE	0.714	0.831
	SIDE	MAE	0.688	0.794
		R^2	0.838	0.795
		RMSE	0.853	0.927
	TS	MAE	0.695	0.741
		R^2	0.856	0.801
		RMSE	0.837	0.997
Gel strength	TOP	MAE	0.472	0.497
		R^2	0.774	0.721
		RMSE	0.610	0.619
	SIDE	MAE	0.350	0.449
		R^2	0.811	0.690
		RMSE	0.435	0.651
	TS	MAE	0.460	0.391
		R^2	0.744	0.691
		RMSE	0.672	0.556

the test set, suggesting potential overfitting. In addition, although the TOP model exhibited the highest R^2 values, it showed the largest prediction errors in both the training and test sets. Therefore, considering prediction accuracy on the test set, the TS model achieved the lowest error rates and demonstrated superior generalization capability. These findings suggest that incorporating both top and side view information more effectively captures the relationship with gel strength.

In the broader context of food quality assessment, various studies have explored the integration of machine learning and analytical technologies to enhance food safety and quality (Breda et al., 2024). Among these, spectroscopy and hyperspectral imaging (HSI) techniques combined with machine learning have been widely used to predict WHC and gel strength. Table 3 summarizes major previous studies that utilized diverse food materials and analytical techniques for predicting WHC and gel strength.

In previous research, for example, HSI has been employed to develop a least squares support vector machine (LS-SVM) model for predicting the WHC of red meat, which demonstrated high predictive accuracy (Kamruzzaman et al., 2016). In addition, a PLS model was developed by applying Raman spectroscopy to pork batter to predict WHC, achieving a relatively high prediction performance with an R^2 value of 0.9611 (Li, H. et al., 2025a). For gel strength, a PLS model based on FT-NIR was applied to gelatin samples and showed a prediction performance of RPD = 1.90 (Duthen et al., 2021). Furthermore, for surimi samples, a PLS model based on HSI-VNIR data was applied, achieving an $R_p^2 = 0.9315$, which indicates very high predictive accuracy (Li, H. et al., 2025b).

However, the practical application of these approaches is limited due to their reliance on expensive equipment and highly specialized personnel. To overcome these constraints, this study proposes a cost-effective alternative: a digital image-based model for predicting 3D printability. The proposed model enables rapid, non-destructive, real-time evaluation; however, several limitations remain. All models exhibited a slight decline in predictive performance on the test dataset compared to the training dataset, which is a common indication of mild overfitting in small datasets (Outrequin et al., 2024). Moreover, the model's predictive accuracy, as indicated by the R^2 values, was somewhat lower than that of the spectroscopy-based methods listed in Table 3. This discrepancy likely stems from methodological differences: spectroscopy quantifies the chemical composition directly, while the image-based approach adopted in this study evaluates surface texture features. Additionally, this study focused solely on texture quantification and additive concentration, omitting variables such as color histograms and shape descriptors.

These findings underscore the potential of image-based models in food texture prediction, while also highlighting the need for future studies to incorporate additional visual and structural descriptors—such as color histograms and shape features—to improve model accuracy and generalizability.

3.4. Variable importance and correlation analysis

In this study, RF-based variable importance analysis was employed to identify key variables influencing printability, while correlation analysis was performed to quantitatively assess the relationships among these variables.

For WHC, the RF analysis achieved the highest predictive performance with the Top view model. As Fig. 7c illustrates, the key variables identified included Contrast, Entropy, TGase concentration, and Correlation. Among these, Contrast and Entropy, derived from GLCM analysis, exhibited the strongest associations with WHC, reflecting variations in surface characteristics and the degree of structural order, respectively. Notably, Contrast and Entropy ranked among the most influential variables, with statistically significant correlations with WHC, as depicted in Fig. 7e. Specifically, Contrast demonstrated a significant negative correlation with WHC ($r = -0.635$, $p < 0.001$), whereas Entropy exhibited a significant positive correlation ($r = 0.514$, $p < 0.001$). Furthermore, Energy ($r = -0.452$, $p < 0.001$) and Homogeneity ($r = -0.549$, $p < 0.001$) showed significant correlations with WHC. These findings underscore the complementary roles of RF and correlation analyses in identifying and validating key variables, particularly Contrast and Entropy, in WHC prediction. This finding suggests that the development of a more compact and robust network structure enhances WHC, leading to smoother surfaces, reduced cracking, and improved printing accuracy. In contrast, surface roughness and printing irregularities can be attributed to moisture loss resulting from diminished protein-water interactions (Dong et al., 2020; Wang et al., 2018).

For gel strength, the RF analysis exhibited the highest predictive performance with the TS model. As depicted in Fig. 7d, the key variables identified were Energy, Contrast, Correlation, TGase concentration, and NaCl concentration. Among these, Energy demonstrated the highest variable importance in the RF analysis, with correlation analysis (Fig. 7f) confirming a significant positive correlation with gel strength ($r = 0.414$, $p < 0.001$). Contrast emerged as the second most influential variable, displaying a significant negative correlation with gel strength ($r = -0.358$, $p < 0.001$), further reinforcing the consistency and reliability of the RF analysis results. Similarly, for gel strength, higher values were associated with improved structural stability, and reduced cracking, consistent with findings from previous studies (Dong et al., 2020; Wei et al., 2024). However, under high salt or TGase conditions, 3D printing performance was adversely affected.

Although Contrast and Entropy were identified as major predictors for WHC, and Energy and Contrast for gel strength, their contributions were not strictly linear. Particularly under high salt or high TGase conditions, high gel strength was not always accompanied by smoother surfaces, indicating that structural compactness does not necessarily equate to favorable surface texture. For instance, under the conditions of 1 % NaCl with 0.4 % TGase and 3 % NaCl with 0.4 % TGase, although relatively high gel strength values were achieved, the printed samples exhibited irregular surface textures and cracking, as visually confirmed in Fig. 4c and e. These findings highlight the context-dependent and nonlinear nature of the relationships between GLCM based texture features and printability outcomes, underscoring the importance of modeling approaches like RF that can capture such complexity.

3.5. SHAP-based interpretation of texture feature contributions

In this study, SHAP analysis was employed to interpret the contribution of texture features extracted from GLCM-based surface images to the prediction of WHC and gel strength. The SHAP visualizations presented in Fig. 8a–c were served as spatial interpretation tools to

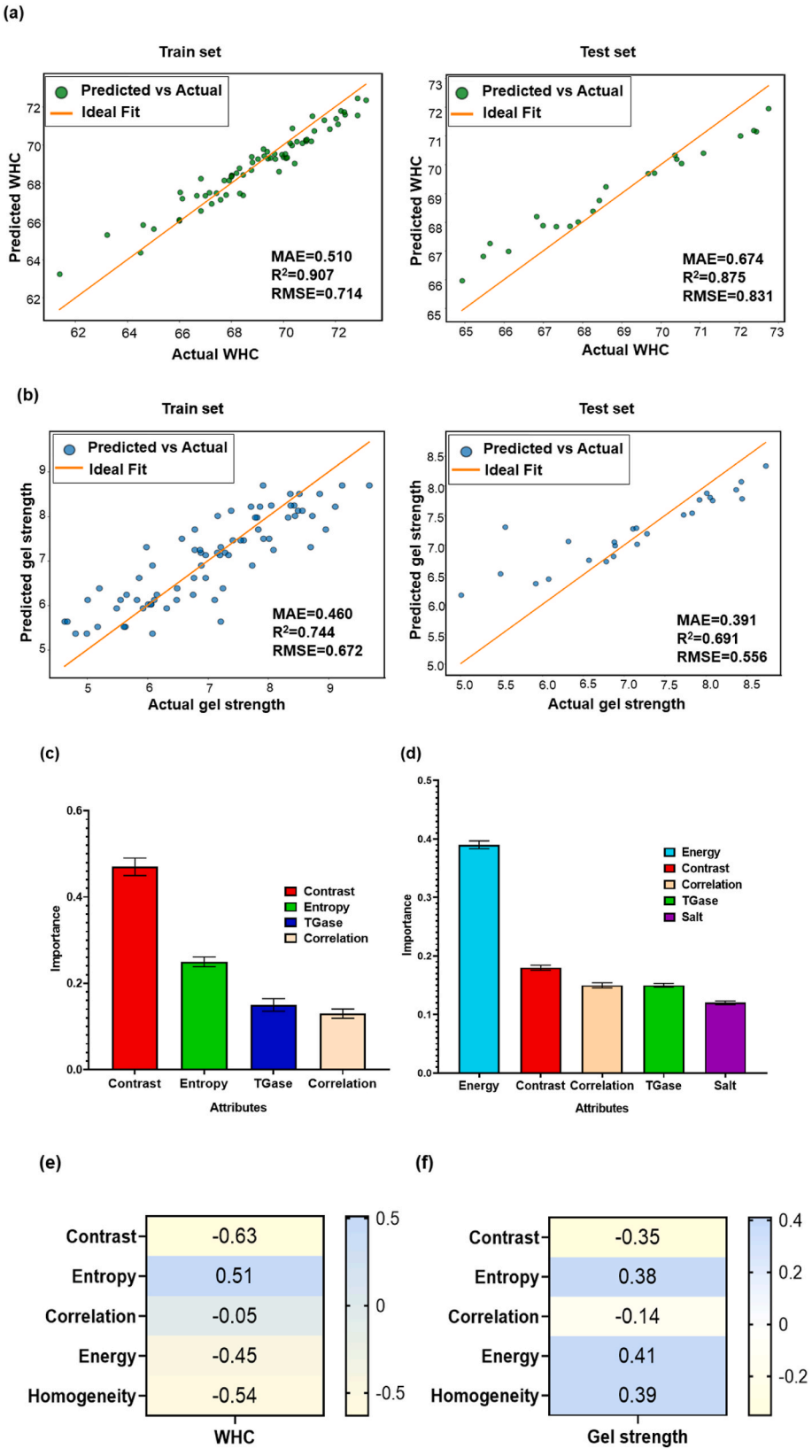

Fig. 7. Prediction performance, variable importance, and correlation analysis for WHC and gel strength prediction. (a) Scatter plots comparing the measured and RF-predicted values for WHC (TOP model) using both training and test sets, (b) Scatter plots comparing the measured and RF-predicted values for gel strength (TS model) using both training and test sets, (c) Feature importance rankings for WHC using the TOP model. (d) Feature importance rankings for gel strength using the TS model, (e) Correlation heatmap for WHC with the TOP model, (f) Correlation heatmap for gel strength with the TS model.

Table 3
Comparison of non-destructive methods for predicting WHC and gel strength in food systems.

Printability	Method	Materials	Data	Algorithm	Main outcomes
WHC	Kamruzzaman et al. (2016)	Red meat	HSI	LS-SVM	$R_p^2 = 0.93$, RPD = 4.09
	Li, H. et al. (2025a)	Pork batter	Raman spectroscopy	PLS	$R_p^2 = 0.9611$, RPD = 3.3988
	Ma et al. (2018)	Cooked pork Sausages	MSI	PLSR	r = 0.832
	Our method	3D-printed surimi	Digital image	RF	$R_p^2 = 0.875$ RMSE = 0.831
Gel strength	Duthen et al. (2021)	Gelatin	FT-NIR	PLS	RPD = 1.90
	Li, H. et al. (2025b)	Minced pork gel + potato starch	Raman spectroscopy	UVE-SVM	$R_p^2 = 0.8508$, RPD = 2.1981
	Xia et al. (2025)	Surimi	HSI-VNIR	PLS	R_p^2 0.9315, RMSEP = 36.1926
	Our method	3D-printed surimi	Digital image	RF	$R_p^2 = 0.691$, RMSE = 0.556

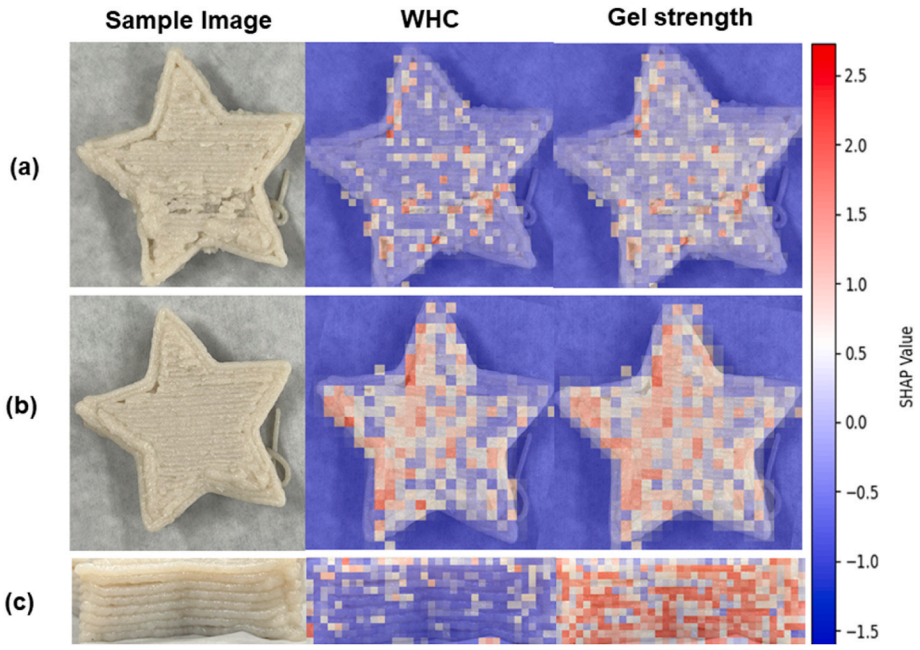

Fig. 8. Example collection of SHAP interpretations for 3D-printed surimi samples: (a) SHAP visualization for WHC and gel strength predictions in a NaCl 3 %, TGase 0 % top-view sample, (b) SHAP visualization for WHC and gel strength predictions in a NaCl 3 %, TGase 0.1 % top-view sample, and (c) SHAP visualization for WHC and gel strength predictions in a NaCl 3 %, TGase 0.3 % side-view sample.

highlight the regions that most influenced the model's predictions.

In the SHAP visualizations, red regions indicate texture features that contribute to an increase in the predicted value, whereas blue regions reflect those that contribute to a decrease. The intensity of the color corresponds to the magnitude of the feature's contribution—darker shades signify a stronger influence on the model's prediction.

Fig. 8a and b presents SHAP visualizations for top view samples containing 0 % and 0.1 % TGase, respectively, under a 3 % NaCl condition. A comparison between the two conditions revealed that as the TGase concentration increased, surface roughness and texture patterns changed, and the surface areas recognized as important by the model also shifted. The distribution of high-contribution regions, indicated in red in the SHAP visualization, increased, while blue regions decreased, suggesting that TGase-induced surface structural changes altered the influence of specific areas on the model's predictions of WHC and gel strength. These changes indicate a shift in the predictive contributions of surface features, with the model reinterpreting which regions are most relevant as TGase concentration increases.

Fig. 8c shows SHAP interpretation results for a side view sample under NaCl 3 % and TGase 0.3 % conditions, where the regions contributing to WHC and gel strength predictions differ distinctly. This observation reflects that the two quality indicators are predicted based on different surface structural features. It indicates that the model utilizes different texture information depending on the input direction, demonstrating that each quality indicator is learned based on distinct visual information. In practice, the TOP model showed the highest predictive performance for WHC, while the TS model, combining both top and side views recorded the best performance for gel strength. These findings can be interpreted as visual validation of the correlation between input directionality and prediction accuracy through SHAP analysis. In conclusion, SHAP visualization goes beyond performance evaluation by quantitatively presenting how texture-based feature contributions are spatially distributed for each quality indicator. This provides meaningful insights for understanding the relationship between surface structure and physicochemical properties of 3D-printed surimi.

Overall, smoother surfaces were associated with improvements in WHC and gel strength. However, SHAP analysis occasionally indicated that certain localized rough or aggregated surface regions contributed positively to the prediction values. This does not imply that surface roughness inherently enhances WHC or gel strength, but rather suggests that the model is highly sensitive to small, localized variations in surface

texture, and that minor irregularities within otherwise smooth surfaces may have been learned as predictive cues. As shown in the experimental results in Section 3.2, samples with high WHC or gel strength often exhibited surface defects, leading to a decrease in overall printability. In this context, the positive contributions observed in SHAP should be interpreted not as indicators of actual improvements in physicochemical properties, but as reflections of the relative patterns and sensitivities learned by the model. SHAP visualizations represent relative feature contributions rather than absolute surface properties, and therefore, localized texture variations may yield high SHAP values even if they are not directly related to improvements in product quality.

4. Conclusions and future work

This study successfully developed a machine learning-based predictive model for evaluating the printability of 3D-printed surimi. We achieved this by quantitatively extracting texture features from digital images using CV techniques. Specifically, a RF regression model, based on GLCM features, effectively analyzed surface textural variations induced by different additive types and concentrations. Our results clearly demonstrate that printability can be accurately predicted solely through non-destructive digital image analysis, a significant advancement over traditional methods.

For WHC prediction, the TOP model demonstrated superior performance, achieving a MAE of 0.674, R^2 of 0.875, and RMSE of 0.831. In contrast, the TS model exhibited higher accuracy for gel strength prediction, yielding a MAE of 0.391, R^2 of 0.691, and RMSE of 0.556. Compared to conventional, destructive, and time-intensive experimental methods, our proposed approach offers a cost-effective and non-destructive alternative that significantly reduces both labor and resource requirements. This innovation represents meaningful progress toward efficient and sustainable food quality assessment in 3D food printing.

Nevertheless, to improve its generalizability, future research should involve large-scale experiments encompassing a broader range of additive combinations. Further validation using diverse datasets, including various fish and meat-based raw materials, is also essential. To further improve predictive performance, diversifying the input features — such as color histograms and shape descriptors — and evaluating alternative machine learning architectures like convolutional neural networks and transformer-based models should be considered. In conclusion, this study not only demonstrates the feasibility of digital image-based printability assessment for 3D-printed foods but also lays crucial groundwork for the refinement and interpretability of machine learning models aimed at quantitative quality prediction. Given the relatively limited application of machine learning technologies within the food industry, the proposed approach offers valuable insights for advancing automated and data-driven quality evaluation in food manufacturing.

CRediT authorship contribution statement

Sol Kim: Writing – review & editing, Writing – original draft, Visualization, Software, Methodology, Investigation, Formal analysis, Data curation, Conceptualization. **Jaehwi Seol:** Writing – review & editing, Validation, Resources. **Eunji Ju:** Writing – review & editing, Formal analysis, Data curation. **Jeonghyeon Pak:** Writing – review & editing, Resources, Investigation, Formal analysis. **Hyoung Il Son:** Writing – review & editing, Supervision. **Soo-Jung Kim:** Writing – review & editing, Supervision, Project administration, Funding acquisition.

Declaration of competing interest

The authors declare that they have no known competing financial interests or personal relationships that could have appeared to influence the work reported in this paper.

Acknowledgment

This work was supported by Korea Institute of Planning and Evaluation for Technology in Food, Agriculture and Forestry (IPET) through Agriculture and Food Convergence Technologies Program for Research Manpower development, funded by Ministry of Agriculture, Food and Rural Affairs (MAFRA) (RS-2024-00402136).

Data availability

Data will be made available on request.

References

Breda, L.S., de Melo Nascimento, J.E., Alves, V., de Toledo, V.d.A.A., de Lima, V.A., Felsner, M.L., 2024. Green and fast prediction of crude protein contents in bee pollen based on digital images combined with random forest algorithm. Food Res. Int. 179, 113958.

Cando, D., Borderías, A.J., Moreno, H., 2016. Combined effect of aminoacids and microbial transglutaminase on gelation of low salt surimi content under high pressure processing. Innov. Food Sci. Emerg. Technol. 36, 10–17. https://doi.org/10.1016/j.ifset.2016.05.010.

Cao, F., Chen, R., Li, Y., Han, R., Li, F., Shi, H., Jiao, Y., 2022. Effects of NaCl and MTGase on printability and gelling properties of extrusion-based 3D printed white croaker (Argyrosomus argentatus) surimi. LWT 164, 113646. https://doi.org/10.1016/j.lwt.2022.113646.

Dong, X., Huang, Y., Pan, Y., Wang, K., Prakash, S., Zhu, B., 2019. Investigation of sweet potato starch as a structural enhancer for three-dimensional printing of Scomberomorus niphonius surimi. J. Texture Stud. 50 (4), 316–324. https://doi.org/10.1111/jtxs.12398.

Dong, X., Pan, Y., Zhao, W., Huang, Y., Qu, W., Pan, J., Qi, H., Prakash, S., 2020. Impact of microbial transglutaminase on 3D printing quality of Scomberomorus niphonius surimi. LWT 124, 109123. https://doi.org/10.1016/j.lwt.2020.109123.

Duthen, S., Levasseur-Garcia, C., Kleiber, D., Violleau, F., Vaca-Garcia, C., Tsuchikawa, S., Raynaud, C.D., Daydé, J., 2021. Using near-infrared spectroscopy to determine moisture content, gel strength, and viscosity of gelatin. Food hydrocoll 115, 106627. https://doi.org/10.1016/j.foodhyd.2021.106627.

Elbadawi, M., Castro, B.M., Gavins, F.K., Ong, J.J., Gaisford, S., Pérez, G., Basit, A.W., Cabalar, P., Goyanes, A., 2020. M3DISEEN: a novel machine learning approach for predicting the 3D printability of medicines. Int. J. Pharm. 590, 119837. https://doi.org/10.1016/j.ijpharm.2020.119837.

Fukuda, S., Yasunaga, E., Nagle, M., Yuge, K., Sardsud, V., Spreer, W., Müller, J., 2014. Modelling the relationship between peel colour and the quality of fresh mango fruit using random forests. J. Food Eng. 131, 7–17. https://doi.org/10.1016/j.jfoodeng.2014.01.007.

Haralick, R.M., Shanmugam, K., Dinstein, I.H., 1973. Textural features for image classification. IEEE Trans. Syst. Man Cybern. 6, 610–621. https://doi.org/10.1109/TSMC.1973.4309314.

Kamruzzaman, M., Makino, Y., Oshita, S., 2016. Hyperspectral imaging for real-time monitoring of water holding capacity in red meat. LWT 66, 685–691. https://doi.org/10.1016/j.lwt.2015.11.021.

Kim, S.M., Wen, Y., Kim, H.W., Park, H.J., 2022. Textural and sensory qualities of low-calorie surimi with carrageenan inserted as a protein substitute using coaxial extrusion 3D food printing. J. Food Eng. 333, 111141. https://doi.org/10.1016/j.jfoodeng.2022.111141.

Lee, J., 2021. A 3D food printing process for the new normal era: a review. Processes 9 (9), 1495. https://doi.org/10.3390/pr9091495.

Li, G., Zhan, J., Hu, Z., Huang, J., Yao, Q., Yuan, C., Chen, J., Hu, Y., 2023. Effects of nano starch-lutein on 3D printing properties of functional surimi: enhancement mechanism of printing effects and anti-oxidation. J. Food Eng. 346, 111431. https://doi.org/10.1016/j.jfoodeng.2023.111431.

Li, H., Sheng, W., Nunekpeku, X., Hu, Y., Chen, Q., 2025a. Prediction of thermal processing effects on gel strength and water holding capacity in pork batter gels: an integrated approach using raman spectroscopy and chemometric techniques. Food Control 175, 111298. https://doi.org/10.1016/j.foodcont.2025.111298.

Li, H., Zhang, W., Nunekpeku, X., Sheng, W., Chen, Q., 2025b. Investigating the change mechanism and quantitative analysis of minced pork gel quality with different starches using Raman spectroscopy. Food hydrocoll 159, 110634. https://doi.org/10.1016/j.foodhyd.2024.110634.

Li, W., Zhang, K., Qin, Y., Li, M., Li, H., Guo, M., Xu, T., Sun, Q., Ji, N., Xie, F., 2025. Effects of sodium chloride on the textural attributes, rheological properties, microstructure, and 3D printing performance of rice starch-curdlan composite gel. Food Chem. 465, 141986. https://doi.org/10.1016/j.foodchem.2024.141986.

Liu, C., Wang, L., Lu, W., Liu, J., Yang, C., Fan, C., Li, Q., Tang, Y., 2022. Computer vision-aided bioprinting for bone research. Bone Res 10 (1), 21. https://doi.org/10.1038/s41413-022-00192-2.

Liu, Y., Sun, Q., Wei, S., Xia, Q., Pan, Y., Ji, H., Deng, C., Hao, J., Liu, S., 2022a. Insight into the correlations among rheological behaviour, protein molecular structure and 3D printability during the processing of surimi from golden pompano (Trachinotus ovatus). Food Chem. 371, 131046. https://doi.org/10.1016/j.foodchem.2021.131046.

Liu, Y., Sun, Q., Wei, S., Xia, Q., Pan, Y., Liu, S., Ji, H., Deng, C., Hao, J., 2022b. LF-NMR as a tool for predicting the 3D printability of surimi-starch systems. Food Chem. 374, 131727. https://doi.org/10.1016/j.foodchem.2021.131727.

Lu, S., Pei, Z., Lu, Q., Li, Q., He, Y., Feng, A., Liu, Z., Xue, C., Liu, J., Lin, X., 2024. Effect of a collagen peptide–fish oil high internal phase emulsion on the printability and gelation of 3D-printed surimi gel inks. Food Chem. 446, 138810. https://doi.org/10.1016/j.foodchem.2024.138810.

Lu, Y., Rai, R., Nitin, N., 2023. Image-based assessment and machine learning-enabled prediction of printability of polysaccharides-based food ink for 3D printing. Food Res. Int. 173, 113384. https://doi.org/10.1016/j.foodres.2023.113384.

Lundberg, S.M., Lee, S.-I., 2017a. Consistent feature attribution for tree ensembles. arXiv preprint arXiv:1706.06060. https://doi.org/10.48550/arXiv.1706.06060.

Lundberg, S.M., Lee, S.-I., 2017b. A unified approach to interpreting model predictions. Adv. Neural Inf. Process. Syst. 30.

Ma, F., Zhang, B., Wang, W., Li, P., Niu, X., Chen, C., Zheng, L., 2018. Potential use of multispectral imaging technology to identify moisture content and water-holding capacity in cooked pork sausages. J. Sci. Food Agri. 98 (5), 1832–1838. https://doi.org/10.1002/jsfa.8659.

Ma, Y., Potappel, J., Chauhan, A., Schutyser, M.A., Boom, R.M., Zhang, L., 2023. Improving 3D food printing performance using computer vision and feedforward nozzle motion control. J. Food Eng. 339, 111277. https://doi.org/10.1016/j.jfoodeng.2022.111277.

Marcucci, A., Gaggiotti, C., Ferarra, L., 2023. A prediction of the printability of concrete through Artificial Neural Networks (ANN). Mater. Today Proc. https://doi.org/10.1016/j.matpr.2023.07.310.

Mutlu, A.C., Boyaci, I.H., Genis, H.E., Ozturk, R., Basaran-Akgul, N., Sanal, T., Evlice, A. K., 2011. Prediction of wheat quality parameters using near-infrared spectroscopy and artificial neural networks. Eur. Food Res. Technol. 233, 267–274. https://doi.org/10.1007/s00217-011-1515-8.

Outrequin, T.C.R., Gamonpilas, C., Siriwatwechakul, W., Sreearunothai, P., 2023. Extrusion-based 3D printing of food biopolymers: a highlight on the important rheological parameters to reach printability. J. Food Eng. 342, 111371. https://doi.org/10.1016/j.jfoodeng.2022.111371.

Outrequin, T.C.R., Gamonpilas, C., Sreearunothai, P., Deepaisarn, S., Siriwatwechakul, W., 2024. Machine learning assisted evaluation of the filament spreading during extrusion-based 3D food printing: impact of the rheological and printing parameters. J. Food Eng. 381, 112166. https://doi.org/10.1016/j.jfoodeng.2024.112166.

Paraskevoudis, K., Karayannis, P., Koumoulos, E.P., 2020. Real-time 3D printing remote defect detection (stringing) with computer vision and artificial intelligence. Processes 8 (11), 1464. https://doi.org/10.3390/pr8111464.

Petsiuk, A.L., Pearce, J.M., 2020. Open source computer vision-based layer-wise 3D printing analysis. Addit. Manuf. 36, 101473. https://doi.org/10.1016/j.addma.2020.101473.

Sun, Y., Sun, J., Zhao, M., Zhao, M., Shi, H., Liu, Z., Zhang, X., Xia, G., 2025. Enhancing gel and 3D printing performance of lipid-enhanced skipjack tuna (Katsuwonus pelamis) surimi via pickering high internal phase emulsion. Food Res. Int. 201, 115649. https://doi.org/10.1016/j.foodres.2024.115649.

Tian, H., Wang, K., Lan, H., Wang, Y., Hu, Z., Zhao, L., 2021. Effect of hybrid gelator systems of beeswax-carrageenan-xanthan on rheological properties and printability of litchi inks for 3D food printing. Food hydrocoll 113, 106482. https://doi.org/10.1016/j.foodhyd.2020.106482.

Wang, L., Zhang, M., Bhandari, B., Yang, C., 2018. Investigation on fish surimi gel as promising food material for 3D printing. J. Food Eng. 220, 101–108. https://doi.org/10.1016/j.jfoodeng.2017.02.029.

Wei, Y., Wang, C., Guo, X., Wang, Z., Deng, X., Zhang, J., 2024. Enhancement of micron fish bone on gelling and 3D printing properties of northern pike (Esox lucius) low-salt surimi. LWT 208, 116709. https://doi.org/10.1016/j.lwt.2024.116709.

Wu, J., Zhu, H., Li, C., 2024. Potential sources of novel proteins suitable for use as ingredients in 3D food printing, along with some of the food safety challenges. Int. J. Gastron. Food Sci. 37, 100983. https://doi.org/10.1016/j.ijgfs.2024.100983.

Xia, Y., Xiao, X., Adade, S.Y.-S.S., Xi, Q., Wu, J., Xu, Y., Chen, Q., Chen, Q., 2025. Physicochemical properties and gel quality monitoring of surimi during thermal processing using hyperspectral imaging combined with deep learning. Food Control 175, 111258. https://doi.org/10.1016/j.foodcont.2025.111258.

Yam, K.L., Papadakis, S.E., 2004. A simple digital imaging method for measuring and analyzing color of food surfaces. J. Food Eng. 61 (1), 137–142. https://doi.org/10.1016/S0260-8774(03)00195-X.

Yang, F., Zhang, M., Bhandari, B., 2017. Recent development in 3D food printing. Crit. Rev. Food Sci. Nutr. 57 (14), 3145–3153. https://doi.org/10.1080/10408398.2015.1094732.

Yu, N., Yang, F., Gong, H., Zhou, J., Jie, C., Wang, W., Chen, X., Sun, L., 2022. Gel & three-dimensional printing properties of sheep plasma protein-surimi induced by transglutaminase. J. Food Eng. 323, 111006. https://doi.org/10.1016/j.jfoodeng.2022.111006.